LEAST-SQUARES RECONSTRUCTION OF PRESSURE FROM PERPENDICULAR INTERSECTING PIV FIELDS IN A TURBULENT SEPARATION BUBBLE

Matthew Harker[a], **Giuseppe Di Labbio**[b], **Louis Dufresne**[b]
Control and Robotics Laboratory,
Department of Systems Engineering[a]
Laboratory of Fluid Mechanics and Applications,
Department of Mechanical Engineering[b]
École de technologie supérieure
Montréal, QC H3C 1K3, Canada
matthew.harker@etsmtl.ca,
giuseppe.dilabbio@etsmtl.ca, louis.dufresne@etsmtl.ca

Arnaud Le Floc'h, Nan Hu, Michaela Herr
Department of Wind Energy,
Institute of Aerodynamics and Flow Technology
German Aerospace Center (DLR)
38108 Braunschweig, Germany
arnaud.lefloch@dlr.de,
nan.hu@dlr.de, michaela.herr@dlr.de

Jérôme Vétel
Laboratory of Fluid Dynamics
Department of Mechanical Engineering
Polytechnique Montréal
Montréal, QC H3T 1J4, Canada
jerome.vetel@polymtl.ca

ABSTRACT

We present a novel technique to reconstruct the pressure fields from two dimensions-two components Particle Image Velocimetry ($2D-2C$ PIV) data on a turbulent separation bubble at $Re_\theta = 5000$ investigated by Le Floc'h *et al.* (2018). Using the equal potential at the intersection of perpendicular velocity fields, the newly tested algorithm from Harker (2025) is five orders of magnitude faster than the state-of-the-art. It has already proven successful with synthetic data, including the addition of synthetic noise. This approach enables us to analyze the dynamic pressure response not only at the wall but also in terms of coherent structures.

WALL PRESSURE OF SEPARATED FLOWS

In a recent study, Le Floc'h *et al.* (2024) reviewed the wall pressure statistics of turbulent flow separation using datasets from a flat plate and two airfoils, namely the $DU96-W-180$ and $NACA$ 4418 geometries. Spectral and time-domain analyses showed consistent markers of separation: low-frequency breathing motions, high-frequency recirculation signatures, and distinct skewness/kurtosis patterns. A novel phase-based method with neighboring sensors captured the transition in convection from downstream vortex shedding to upstream backflow. Their results further demonstrated that wall pressure measurements alone is a promising tool to effectively distinguish between attached, weak, and massive separation, supporting improved aerodynamic and aeroacoustic modeling. Indeed, a key objective at DLR Braunschweig is the detection and monitoring of detrimental conditions that may occur on wind turbine blades. To effectively train a machine learning algorithm, we must be able to derive the turbulent flow separation topology from wall-based measurements.

To support this long-term research goal, the present study focuses on pressure directly computed from velocity fields obtained via PIV measurements arranged in a T-shaped configuration.

This analysis is motivated by several factors: First, pressure fluctuations reconstructed from PIV data can be used to predict far-field noise (e.g. like trailing edge noise) through an acoustic analogy, as demonstrated by Chen & Ye (2024); Pröbsting *et al.* (2015). Moreover, Chen & Ye (2024) presented a fast and optimized method for reconstructing pressure fields and predicting far-field noise in flows past tandem cylinders using time-resolved PIV. After applying proper orthogonal decomposition (POD) for denoising and solving the Poisson equation, the study achieves accurate pressure and noise predictions that align well with reference measurements. This approach provided valuable insights into flow-induced noise mechanisms that are of interest for application like in Wind Energy (Le Floc'h *et al.*, 2024), where flow separation noise remains a major challenge. Second, exploring the relationship between field and wall pressure is of particular interest. While structures associated with negative pressure fluctuations are known to interact directly with the wall (Abe, 2017), Le Floc'h *et al.* (2024) observed positively skewed fluctuations near the onset of separation that currently lack a clear structural model. Finally, a recent contradiction has emerged regarding wall-pressure signatures near incipient detachment. Whereas Mohammed-Taifour & Weiss (2016); Le Floc'h (2021) found positive fluctuations to drive an expansion of the recirculation region, Wang *et al.* (2024) argued for a corresponding negative signature when modeling the response using a low-frequency SPOD mode. Therefore, PIV-based pressure reconstruction may help clarify this issue.

FIELD PRESSURE RECONSTRUCTION

The reconstruction of the pressure potential from the velocity data is generally an inverse problem. It is therefore important to properly model the influence of measurement error on the reconstruction problem, for example, by assuming Gaussian measurement noise and formulating the corresponding least-squares cost-function. For a measured velocity field in matrix form, $(\hat{\mathsf{U}}, \hat{\mathsf{V}})$, we have,

$$\hat{\mathsf{U}} = \mathsf{U} + \Delta_u \qquad \text{and} \qquad \hat{\mathsf{V}} = \mathsf{V} + \Delta_v \,, \tag{1}$$

where (U, V) is the true velocity field, and (Δ_u, Δ_v) are Gaussian random variables. Any estimate of the true velocity field should therefore minimize the cost-function,

$$\varepsilon = \|\Delta_u\|_{\mathrm{F}}^2 + \|\Delta_v\|_{\mathrm{F}}^2 = \left\|\hat{\mathsf{U}} - \mathsf{U}\right\|_{\mathrm{F}}^2 + \left\|\hat{\mathsf{V}} - \mathsf{V}\right\|_{\mathrm{F}}^2 \,. \tag{2}$$

Further, the velocity field is derived from the unknown pressure distribution, P, such that,

$$\mathsf{U} = \frac{\partial}{\partial x}\mathsf{P} \qquad \text{and} \qquad \mathsf{V} = \frac{\partial}{\partial y}\mathsf{P} \,. \tag{3}$$

When the velocity field is derived from a potential function, the field is said to be integrable, and the potential can be reconstructed by ordinary calculus. With measurement data, the velocity field is corrupted by noise, and is generally not integrable. An optimization based approach, such as the method of least-squares, is necessary to obtain an approximate solution to the problem. This approach also enables the reconstruction to be accomplished with constraints on the solution which have the effect of regularization. In the measurement context, the problem of differential calculus must be appropriately discretized. The foundation of the proposed algorithm is the concept of the numerical differentiation matrix, which enables fast and accurate solutions of ODE and PDE.

Numerical Differentiation Matrices

Rather than relying on classic finite difference or finite element methods, which are notoriously computationally expensive, the rectangular structure of digital images allows for great computational improvements due to the numerical differentiation matrices (Harker & O'Leary, 2015). This matrix-based approach stems from classic numerical differentiation formulas, such as,

$$f'(x_k) \approx \tfrac{1}{2h} f(x_{k-1}) + \tfrac{1}{2h} f(x_{k+1}) \,. \tag{4}$$

where $h = x_{k+1} - x_k = x_k - x_{k-1}$. Since the extent of the data is finite, we must also introduce end-point formulas (Burden & Faires, 2005). Because such numerical differentiation formulas generally comprise coefficients of function values, these terms can be factored into matrix form to obtain matrices such as,

$$\mathsf{D} = \frac{1}{2h}\begin{bmatrix} -3 & 4 & -1 & 0 & 0 & 0 \\ -1 & 0 & -1 & 0 & 0 & 0 \\ 0 & -1 & 0 & 1 & 0 & 0 \\ 0 & 0 & -1 & 0 & 1 & 0 \\ 0 & 0 & 0 & -1 & 0 & 1 \\ 0 & 0 & 0 & 1 & -4 & 3 \end{bmatrix} , \tag{5}$$

where even spacing, h, between function values is assumed. These formulas are derived from a second order interpolation polynomial, and are hence second order accurate. Given a vector of function values, f, we thereby obtain a vector of numerical derivatives as,

$$f' \approx \mathsf{D} f \,, \tag{6}$$

thus facilitating a matrix-algebraic formulation and solution of inverse problems such as potential reconstruction from velocity measurements. The partial derivatives in Equation (3) can correspondingly be calculated numerically as,

$$\mathsf{U} = \mathsf{D}_x \mathsf{P} \qquad \text{and} \qquad \mathsf{V} = \mathsf{P}\mathsf{D}_y^{\mathrm{T}} \,, \tag{7}$$

where the transposed matrix $\mathsf{D}_y^{\mathrm{T}}$ effects differentiation along the matrix rows. In general, numerical differentiation matrices can be constructed with arbitrary interpolation functions (polynomial, trigonometric, exponential) over arbitrary spacing.

Constraint Matrices

As is well known, a function that is reconstructed from gradient information is unique only up to a constant of integration. This constant can be fixed in a number of ways, whereby, in a very general setting, we can fix this value by means of linear constraints such as the integral of the curve over an interval of interest. For the proposed reconstruction algorithm, we investigate linear constraints on a discretized surface, P, of the form,

$$a^{\mathrm{T}} \mathsf{P} b = \alpha \,. \tag{8}$$

In the same vein as numerical differentiation formulas, this form of constraint generally allows for the discretization of linear operators as constraints. Such constraints can therefore describe approximations to function values, derivatives, integrals, averages, etc. For example, if we use simple coordinate vectors, $a = e_i$ and $b = e_j$, we obtain the value constraint, $p_{ij} = \alpha$. In a similar manner, if we choose,

$$a^{\mathrm{T}} = \tfrac{1}{N}\begin{bmatrix} 0 \cdots 0 \; 1 \cdots 1 \; 0 \cdots 0 \end{bmatrix} \tag{9}$$

$$b^{\mathrm{T}} = \tfrac{1}{2}\begin{bmatrix} 0 \cdots 0 \; 1 \; 1 \; 0 \cdots 0 \end{bmatrix} \,, \tag{10}$$

where N is the number of ones in the vector a^{T}, then the resulting constraint is upon the average value along a line segment that is halfway between the indices of b where the non-zero values appear. In the case where we impose multiple constraints along the columns of the matrix P and the same constraint along the rows of P, we have N constraints of the form,

$$q_i^{\mathrm{T}} \mathsf{P} c = \alpha_i \,. \tag{11}$$

In this manner, all such constraints can be stacked together into matrix form as,

$$\mathsf{Q}^{\mathrm{T}} \mathsf{P} c = \alpha \,, \tag{12}$$

where,

$$\mathsf{Q} = \left[q_1 \; q_2 \; \cdots \; q_N \right] \; . \tag{13}$$

For the purposes of coupling two separate surfaces, we can equate such constraints, such that the linear operator that they define has equal values for both surfaces, in which case the constraints take the form,

$$\mathsf{Q}_1^{\mathrm{T}} \mathsf{P}_1 c_1 = \mathsf{Q}_2^{\mathrm{T}} \mathsf{P}_2 c_2 \; . \tag{14}$$

Constrained Potential Reconstruction

The cost function for the potential reconstruction is derived in Equation (2) with partial derivatives as in Equation (7). The constraints between the horizontal and vertical planes as well as the mean value constraint are introduced by means of Lagrange multipliers, λ and ζ, to yield the cost function,

$$\begin{aligned} \varepsilon\left(\mathsf{P}_{\mathrm{h}}, \mathsf{P}_{\mathrm{v}}, \lambda, \zeta\right) = \tfrac{1}{2}\left\|\mathsf{D}_x \mathsf{P}_{\mathrm{h}} - \hat{\mathsf{U}}_{\mathrm{h}}\right\|_{\mathrm{F}}^2 + \tfrac{1}{2}\left\|\mathsf{P}_{\mathrm{h}} \mathsf{D}_z^{\mathrm{T}} - \hat{\mathsf{V}}_{\mathrm{h}}\right\|_{\mathrm{F}}^2 \\ + \tfrac{1}{2}\left\|\mathsf{D}_{x'} \mathsf{P}_{\mathrm{v}} - \hat{\mathsf{U}}_{\mathrm{v}}\right\|_{\mathrm{F}}^2 + \tfrac{1}{2}\left\|\mathsf{P}_{\mathrm{v}} \mathsf{D}_y^{\mathrm{T}} - \hat{\mathsf{V}}_{\mathrm{v}}\right\|_{\mathrm{F}}^2 \\ -\lambda^{\mathrm{T}}\left(\mathsf{Q}_{\mathrm{h}}^{\mathrm{T}} \mathsf{P}_{\mathrm{h}} c_{\mathrm{h}} - \mathsf{Q}_{\mathrm{v}}^{\mathrm{T}} \mathsf{P}_{\mathrm{v}} c_{\mathrm{v}}\right) - \zeta\left(e^{\mathrm{T}} \mathsf{P}_{\mathrm{h}} e + e^{\mathrm{T}} \mathsf{P}_{\mathrm{v}} e\right) \; . \end{aligned} \tag{15}$$

In order to optimize this constrained cost-function, we take the partial derivatives with respect to the unknowns, and equate them to zero. To this end, in keeping with the matrix based approach, we differentiate with respect to the pressure matrices (Schönemann, 1985) to obtain,

$$\begin{aligned} \varepsilon \mathsf{P}_{\mathrm{h}} &= \mathsf{D}_x^{\mathrm{T}}\left(\mathsf{D}_x \mathsf{P}_{\mathrm{h}} - \hat{\mathsf{U}}_{\mathrm{h}}\right) + \left(\mathsf{P}_{\mathrm{h}} \mathsf{D}_z^{\mathrm{T}} - \hat{\mathsf{V}}_{\mathrm{h}}\right) \mathsf{D}_z - \mathsf{Q}_{\mathrm{h}} \lambda c_{\mathrm{h}}^{\mathrm{T}} - \zeta e e^{\mathrm{T}} \\ \varepsilon \mathsf{P}_{\mathrm{v}} &= \mathsf{D}_{x'}^{\mathrm{T}}\left(\mathsf{D}_{x'} \mathsf{P}_{\mathrm{v}} - \hat{\mathsf{U}}_{\mathrm{v}}\right) + \left(\mathsf{P}_{\mathrm{v}} \mathsf{D}_y^{\mathrm{T}} - \hat{\mathsf{V}}_{\mathrm{v}}\right) \mathsf{D}_y + \mathsf{Q}_{\mathrm{v}} \lambda c_{\mathrm{v}}^{\mathrm{T}} - \zeta e e^{\mathrm{T}} \end{aligned} \tag{16}$$

We further differentiate with respect to the Lagrange multipliers, λ and ζ, to recover the constraint equations, which are to be solved simultaneously. The first pair of equations are effectively the gradient matrices of the cost function with respect to the unknown potentials, P_{h} and P_{v}, so we equate them to zero matrices, and rearrange to obtain,

$$\begin{aligned} \mathsf{D}_x^{\mathrm{T}} \mathsf{D}_x \mathsf{P}_{\mathrm{h}} + \mathsf{P}_{\mathrm{h}} \mathsf{D}_z^{\mathrm{T}} \mathsf{D}_z &= \mathsf{D}_x^{\mathrm{T}} \hat{\mathsf{U}}_{\mathrm{h}} + \hat{\mathsf{V}}_{\mathrm{h}} \mathsf{D}_z + \mathsf{Q}_{\mathrm{h}} \lambda c_{\mathrm{h}}^{\mathrm{T}} + \zeta e e^{\mathrm{T}} \\ \mathsf{D}_{x'}^{\mathrm{T}} \mathsf{D}_{x'} \mathsf{P}_{\mathrm{v}} + \mathsf{P}_{\mathrm{v}} \mathsf{D}_y^{\mathrm{T}} \mathsf{D}_y &= \mathsf{D}_{x'}^{\mathrm{T}} \hat{\mathsf{U}}_{\mathrm{v}} + \hat{\mathsf{V}}_{\mathrm{v}} \mathsf{D}_y - \mathsf{Q}_{\mathrm{v}} \lambda c_{\mathrm{v}}^{\mathrm{T}} + \zeta e e^{\mathrm{T}} \end{aligned} \tag{17}$$

These equations are Sylvester matrix equations, respectively in the unknowns, P_{h} and P_{v}. They are, however, coupled by the constraints, and therefore by the Lagrange multipliers, λ and ζ.

In order to solve the four equations (two matrix equations and the two vector constraint equations), the proposed strategy is to solve the two matrix equations for the pressure matrices as functions of the Lagrange multipliers, and then substitute these equations into the constraint equations in order to solve for the Lagrange multipliers. To address the matrix equations, we compute the eigendecompositions of the matrix equations as,

$$\mathsf{D}_x^{\mathrm{T}} \mathsf{D}_x = \mathsf{S}_{\mathrm{h}} \Lambda_{\mathrm{h}} \mathsf{S}_{\mathrm{h}}^{\mathrm{T}} \qquad \mathsf{D}_z^{\mathrm{T}} \mathsf{D}_z = \mathsf{T}_{\mathrm{h}} \mathsf{M}_{\mathrm{h}} \mathsf{T}_{\mathrm{h}}^{\mathrm{T}} \tag{18}$$

$$\mathsf{D}_{x'}^{\mathrm{T}} \mathsf{D}_{x'} = \mathsf{S}_{\mathrm{v}} \Lambda_{\mathrm{v}} \mathsf{S}_{\mathrm{v}}^{\mathrm{T}} \qquad \mathsf{D}_y^{\mathrm{T}} \mathsf{D}_y = \mathsf{T}_{\mathrm{v}} \mathsf{M}_{\mathrm{v}} \mathsf{T}_{\mathrm{v}}^{\mathrm{T}} \tag{19}$$

Substituting these decompositions into the matrix equations, we obtain,

$$\begin{aligned} \mathsf{S}_{\mathrm{h}} \Lambda_{\mathrm{h}} \mathsf{S}_{\mathrm{h}}^{\mathrm{T}} \mathsf{P}_{\mathrm{h}} + \mathsf{P}_{\mathrm{h}} \mathsf{T}_{\mathrm{h}} \mathsf{M}_{\mathrm{h}} \mathsf{T}_{\mathrm{h}}^{\mathrm{T}} &= \mathsf{D}_x^{\mathrm{T}} \hat{\mathsf{U}}_{\mathrm{h}} + \hat{\mathsf{V}}_{\mathrm{h}} \mathsf{D}_z + \mathsf{Q}_{\mathrm{h}} \lambda c_{\mathrm{h}}^{\mathrm{T}} + \zeta e e^{\mathrm{T}} \\ \mathsf{S}_{\mathrm{v}} \Lambda_{\mathrm{v}} \mathsf{S}_{\mathrm{v}}^{\mathrm{T}} \mathsf{P}_{\mathrm{v}} + \mathsf{P}_{\mathrm{v}} \mathsf{T}_{\mathrm{v}} \mathsf{M}_{\mathrm{v}} \mathsf{T}_{\mathrm{v}}^{\mathrm{T}} &= \mathsf{D}_{x'}^{\mathrm{T}} \hat{\mathsf{U}}_{\mathrm{v}} + \hat{\mathsf{V}}_{\mathrm{v}} \mathsf{D}_y - \mathsf{Q}_{\mathrm{v}} \lambda c_{\mathrm{v}}^{\mathrm{T}} + \zeta e e^{\mathrm{T}} \end{aligned} \tag{20}$$

Since the following development involves applying the same manipulations to both planes, yielding identical equations save for the h and v subscripts, we follow the development for only the horizontal plane. We pre-multiply the first equation by $\mathsf{S}_{\mathrm{h}}^{\mathrm{T}}$ and post-multiply by T_{h}, and (correspondingly, we pre-multiply the second equation by $\mathsf{S}_{\mathrm{v}}^{\mathrm{T}}$ and post-multiply by T_{v}) to obtain,

$$\begin{aligned} \Lambda_{\mathrm{h}} \mathsf{S}_{\mathrm{h}}^{\mathrm{T}} \mathsf{P}_{\mathrm{h}} \mathsf{T}_{\mathrm{h}} + \mathsf{S}_{\mathrm{h}}^{\mathrm{T}} \mathsf{P}_{\mathrm{h}} \mathsf{T}_{\mathrm{h}} \mathsf{M}_{\mathrm{h}} = \mathsf{S}_{\mathrm{h}}^{\mathrm{T}} \mathsf{D}_x^{\mathrm{T}} \hat{\mathsf{U}}_{\mathrm{h}} \mathsf{T}_{\mathrm{h}} + \mathsf{S}_{\mathrm{h}}^{\mathrm{T}} \hat{\mathsf{V}}_{\mathrm{h}} \mathsf{D}_z \mathsf{T}_{\mathrm{h}} \\ + \mathsf{S}_{\mathrm{h}}^{\mathrm{T}} \mathsf{Q}_{\mathrm{h}} \lambda c_{\mathrm{h}}^{\mathrm{T}} \mathsf{T}_{\mathrm{h}} + \zeta \mathsf{S}_{\mathrm{h}}^{\mathrm{T}} e e^{\mathrm{T}} \mathsf{T}_{\mathrm{h}} \end{aligned} \tag{21}$$

We next make the orthogonal substitution,

$$\mathsf{Z}_{\mathrm{h}} = \mathsf{S}_{\mathrm{h}}^{\mathrm{T}} \mathsf{P}_{\mathrm{h}} \mathsf{T}_{\mathrm{h}} \; . \tag{22}$$

To this end, in the matrix equations, the coefficient matrices of Z_{h} and Z_{v} are diagonal, which leads to the simplification,

$$\Lambda_{\mathrm{h}} \mathsf{Z}_{\mathrm{h}} + \mathsf{Z}_{\mathrm{h}} \mathsf{M}_{\mathrm{h}} = \mathsf{K}_{\mathrm{h}} \circ \mathsf{Z}_{\mathrm{h}} \; , \tag{23}$$

where $\circ$ indicates the Hadamard (element-wise) product, and the matrix K_{h} (and K_{v}) is given as,

$$\mathsf{K}_{\mathrm{v}} = \lambda_{\mathrm{v}} e^{\mathrm{T}} + e \mu_{\mathrm{v}}^{\mathrm{T}} \; . \tag{24}$$

where λ_{v} and $\mu_{\mathrm{v}}^{\mathrm{T}}$, are vectors containing the eigenvalues of the corresponding matrices. To simplify the expressions, we then define,

$$\mathsf{F}_{\mathrm{h}} = \mathsf{S}_{\mathrm{h}}^{\mathrm{T}} \mathsf{D}_x^{\mathrm{T}} \hat{\mathsf{U}}_{\mathrm{h}} \mathsf{T}_{\mathrm{h}} + \mathsf{S}_{\mathrm{h}}^{\mathrm{T}} \hat{\mathsf{V}}_{\mathrm{h}} \mathsf{D}_z \mathsf{T}_{\mathrm{h}} \; . \tag{25}$$

With these modifications, the equation(s) read,

$$\mathsf{K}_{\mathrm{h}} \circ \mathsf{Z}_{\mathrm{h}} = \mathsf{F}_{\mathrm{h}} + \mathsf{S}_{\mathrm{h}}^{\mathrm{T}} \mathsf{Q}_{\mathrm{h}} \lambda c_{\mathrm{h}}^{\mathrm{T}} \mathsf{T}_{\mathrm{h}} + \zeta \mathsf{S}_{\mathrm{h}}^{\mathrm{T}} e e^{\mathrm{T}} \mathsf{T}_{\mathrm{h}}$$

Given that the eigendecompositions are derived from numerical differentiation matrices, they each have an eigenvalue of zero associated with the fact that the numerical derivative of a constant function must vanish, i.e., $\mathsf{D}_x(ce) = 0$. Assuming that the eigenvalues are ordered in ascending magnitude, the $(1,1)$ entries of the matrices K_{h} and K_{v} are zero, which means that the coefficients of the $(1,1)$ entries of the matrices Z_{h} and Z_{v} are zero, and thereby the corresponding entries cannot be determined by the matrix equations (they are effectively constants of integration).

To satisfy the two equations for the $(1,1)$ entries, we have correspondingly the equations,

$$e_1^{\mathrm{T}} \mathsf{F}_{\mathrm{h}} e_1 + e_1^{\mathrm{T}} \mathsf{S}_{\mathrm{h}}^{\mathrm{T}} \mathsf{Q}_{\mathrm{h}} \lambda c_{\mathrm{h}}^{\mathrm{T}} \mathsf{T}_{\mathrm{h}} e_1 + \zeta e_1^{\mathrm{T}} \mathsf{S}_{\mathrm{h}}^{\mathrm{T}} e e^{\mathrm{T}} \mathsf{T}_{\mathrm{h}} e_1 = 0 \tag{26}$$

$$e_1^{\mathrm{T}} \mathsf{F}_{\mathrm{v}} e_1 - e_1^{\mathrm{T}} \mathsf{S}_{\mathrm{v}}^{\mathrm{T}} \mathsf{Q}_{\mathrm{v}} \lambda c_{\mathrm{v}}^{\mathrm{T}} \mathsf{T}_{\mathrm{v}} e_1 + \zeta e_1^{\mathrm{T}} \mathsf{S}_{\mathrm{v}}^{\mathrm{T}} e e^{\mathrm{T}} \mathsf{T}_{\mathrm{v}} e_1 = 0 \tag{27}$$

To resolve this issue with the remaining matrix entries, we define the Hadamard pseudo-inverse as the matrix,

$$\mathsf{A}^{\circ+} = \left[\hat{a}_{ij}\right] \quad \text{where} \quad \hat{a}_{ij} = \begin{cases} a_{ij}^{-1} & \text{for} \quad a_{ij} \neq 0 \\ 0 & \text{for} \quad a_{ij} = 0 \end{cases} . \tag{28}$$

Pre-multiplying both sides of the matrix equation(s) by the corresponding Hadamard pseudo-inverses,

$$\begin{aligned} \mathsf{Z}_\mathrm{h} =& z_\mathrm{h} e_1 e_1^\mathrm{T} + \mathsf{K}_\mathrm{h}^{\circ+} \circ \mathsf{F}_\mathrm{h} + \mathsf{K}_\mathrm{h}^{\circ+} \circ \left(\mathsf{S}_\mathrm{h}^\mathrm{T} \mathsf{Q}_\mathrm{h} \lambda c_\mathrm{h}^\mathrm{T} \mathsf{T}_\mathrm{h}\right) \\ &+ \zeta \mathsf{K}_\mathrm{h}^{\circ+} \circ \left(\mathsf{S}_\mathrm{h}^\mathrm{T} e e^\mathrm{T} \mathsf{T}_\mathrm{h}\right) . \end{aligned} \tag{29}$$

Here, the terms corresponding to the values z_h and z_v lie in the null space of the Hadamard product, and correspond to constants of integration. Finally, by inverting the transform in Equation (22), we obtain,

$$\begin{aligned} \mathsf{P}_\mathrm{h} =& z_\mathrm{h} \mathsf{S}_\mathrm{h} e_1 e_1^\mathrm{T} \mathsf{T}_\mathrm{h}^\mathrm{T} + \mathsf{S}_\mathrm{h} \left(\mathsf{K}_\mathrm{h}^{\circ+} \circ \mathsf{F}_\mathrm{h}\right) \mathsf{T}_\mathrm{h}^\mathrm{T} \\ &+ \mathsf{S}_\mathrm{h} \left(\mathsf{K}_\mathrm{h}^{\circ+} \circ \left(\mathsf{S}_\mathrm{h}^\mathrm{T} \mathsf{Q}_\mathrm{h} \lambda c_\mathrm{h}^\mathrm{T} \mathsf{T}_\mathrm{h}\right)\right) \mathsf{T}_\mathrm{h}^\mathrm{T} \\ &+ \zeta \mathsf{S}_\mathrm{h} \left(\mathsf{K}_\mathrm{h}^{\circ+} \circ \left(\mathsf{S}_\mathrm{h}^\mathrm{T} e e^\mathrm{T} \mathsf{T}_\mathrm{h}\right)\right) \mathsf{T}_\mathrm{h}^\mathrm{T} . \end{aligned} \tag{30}$$

These two relations give the expression for the pressure distributions in terms of the Lagrange multipliers. Defining the matrices,

$$\hat{\mathsf{F}}_\mathrm{h} = \mathsf{S}_\mathrm{h} \left(\mathsf{K}_\mathrm{h}^{\circ+} \circ \mathsf{F}_\mathrm{h}\right) \mathsf{T}_\mathrm{h}^\mathrm{T} \tag{31}$$

$$\mathsf{G}_\mathrm{h} = \mathsf{S}_\mathrm{h} e_1 e_1^\mathrm{T} \mathsf{T}_\mathrm{h}^\mathrm{T} \tag{32}$$

$$\mathsf{H}_\mathrm{h} = \mathsf{S}_\mathrm{h} \left(\mathsf{K}_\mathrm{h}^{\circ+} \circ \left(\mathsf{S}_\mathrm{h}^\mathrm{T} e e^\mathrm{T} \mathsf{T}_\mathrm{h}\right)\right) \mathsf{T}_\mathrm{h}^\mathrm{T} , \tag{33}$$

with similar definitions for $\hat{\mathsf{F}}_\mathrm{v}$, G_v, and H_v, the expressions for the pressure matrices can be written as,

$$\begin{aligned} \mathsf{P}_\mathrm{h} =& \\ & \hat{\mathsf{F}}_\mathrm{h} + z_\mathrm{h} \mathsf{G}_\mathrm{h} + \mathsf{S}_\mathrm{h} \left(\mathsf{K}_\mathrm{h}^{\circ+} \circ \left(\mathsf{S}_\mathrm{h}^\mathrm{T} \mathsf{Q}_\mathrm{h} \lambda c_\mathrm{h}^\mathrm{T} \mathsf{T}_\mathrm{h}\right)\right) \mathsf{T}_\mathrm{h}^\mathrm{T} + \zeta \mathsf{H}_\mathrm{h} \end{aligned} \tag{34}$$

$$\begin{aligned} \mathsf{P}_\mathrm{v} =& \\ & \hat{\mathsf{F}}_\mathrm{v} + z_\mathrm{v} \mathsf{G}_\mathrm{v} - \mathsf{S}_\mathrm{v} \left(\mathsf{K}_\mathrm{v}^{\circ+} \circ \left(\mathsf{S}_\mathrm{v}^\mathrm{T} \mathsf{Q}_\mathrm{v} \lambda c_\mathrm{v}^\mathrm{T} \mathsf{T}_\mathrm{v}\right)\right) \mathsf{T}_\mathrm{v}^\mathrm{T} + \zeta \mathsf{H}_\mathrm{v} . \end{aligned} \tag{35}$$

Substituting these two expressions into the intersection constraint, we obtain,

$$\begin{aligned} & \mathsf{Q}_\mathrm{h}^\mathrm{T} \left(\hat{\mathsf{F}}_\mathrm{h} + z_\mathrm{h} \mathsf{G}_\mathrm{h} + \mathsf{S}_\mathrm{h} \left(\mathsf{K}_\mathrm{h}^{\circ+} \circ \left(\mathsf{S}_\mathrm{h}^\mathrm{T} \mathsf{Q}_\mathrm{h} \lambda c_\mathrm{h}^\mathrm{T} \mathsf{T}_\mathrm{h}\right)\right) \mathsf{T}_\mathrm{h}^\mathrm{T} + \zeta \mathsf{H}_\mathrm{h}\right) c_\mathrm{h} \\ & - \mathsf{Q}_\mathrm{v}^\mathrm{T} \left(\hat{\mathsf{F}}_\mathrm{v} + z_\mathrm{v} \mathsf{G}_\mathrm{v} - \mathsf{S}_\mathrm{v} \left(\mathsf{K}_\mathrm{v}^{\circ+} \circ \left(\mathsf{S}_\mathrm{v}^\mathrm{T} \mathsf{Q}_\mathrm{v} \lambda c_\mathrm{v}^\mathrm{T} \mathsf{T}_\mathrm{v}\right)\right) \mathsf{T}_\mathrm{v}^\mathrm{T} + \zeta \mathsf{H}_\mathrm{v}\right) c_\mathrm{v} \\ & \qquad = 0 . \end{aligned} \tag{36}$$

In an similar manner, the average value constraint reads,

$$\begin{aligned} & e^\mathrm{T} \left(\hat{\mathsf{F}}_\mathrm{h} + z_\mathrm{h} \mathsf{G}_\mathrm{h} + \mathsf{S}_\mathrm{h} \left(\mathsf{K}_\mathrm{h}^{\circ+} \circ \left(\mathsf{S}_\mathrm{h}^\mathrm{T} \mathsf{Q}_\mathrm{h} \lambda c_\mathrm{h}^\mathrm{T} \mathsf{T}_\mathrm{h}\right)\right) \mathsf{T}_\mathrm{h}^\mathrm{T} + \zeta \mathsf{H}_\mathrm{h}\right) e \\ & + e^\mathrm{T} \left(\hat{\mathsf{F}}_\mathrm{v} + z_\mathrm{v} \mathsf{G}_\mathrm{v} - \mathsf{S}_\mathrm{v} \left(\mathsf{K}_\mathrm{v}^{\circ+} \circ \left(\mathsf{S}_\mathrm{v}^\mathrm{T} \mathsf{Q}_\mathrm{v} \lambda c_\mathrm{v}^\mathrm{T} \mathsf{T}_\mathrm{v}\right)\right) \mathsf{T}_\mathrm{v}^\mathrm{T} + \zeta \mathsf{H}_\mathrm{v}\right) e \\ & \qquad = 0 . \end{aligned} \tag{37}$$

Equations (26) and (27), along with the constraints, Equations (36) and (37), all together represent linear equations in the unknowns, z_h, z_v, ζ, and λ. In order to extract the vector λ from the Hadamard products in which it appears, we note the relation,

$$\mathsf{A}\left(\mathsf{B} \circ \left(\mathsf{C} u a^\mathrm{T}\right)\right) b = \mathsf{A} \operatorname{diag}\left(\mathsf{B}\left(a \circ b\right)\right) \mathsf{C} u . \tag{38}$$

To finally solve these equations simultaneously, we define the matrices and vectors,

$$\mathsf{N}_\mathrm{h} = \mathsf{Q}_\mathrm{h}^\mathrm{T} \mathsf{S}_\mathrm{h} \operatorname{diag}\left(\mathsf{K}_\mathrm{h}^{\circ+} \left(\mathsf{T}_\mathrm{h}^\mathrm{T} c_\mathrm{h} \circ \mathsf{T}_\mathrm{h}^\mathrm{T} c_\mathrm{h}\right)\right) \mathsf{S}_\mathrm{h}^\mathrm{T} \mathsf{Q}_\mathrm{h} \tag{39}$$

$$w_\mathrm{h} = \mathsf{Q}_\mathrm{h}^\mathrm{T} \mathsf{S}_\mathrm{h} \operatorname{diag}\left(\mathsf{K}_\mathrm{h}^{\circ+} \left(\mathsf{T}_\mathrm{h}^\mathrm{T} c_\mathrm{h} \circ \mathsf{T}_\mathrm{h}^\mathrm{T} e\right)\right) \mathsf{S}_\mathrm{h}^\mathrm{T} e , \tag{40}$$

with similar definitions for N_v and w_v. We thereby obtain a linear system of equations of the form,

$$\mathsf{W} \psi = -g , \tag{41}$$

where the matrix W is given as,

$$\mathsf{W} = \begin{bmatrix} \mathsf{Q}_\mathrm{h}^\mathrm{T} \mathsf{G}_\mathrm{h} c_\mathrm{h} & -\mathsf{Q}_\mathrm{v}^\mathrm{T} \mathsf{G}_\mathrm{v} c_\mathrm{v} & \mathsf{Q}_\mathrm{h}^\mathrm{T} \mathsf{H}_\mathrm{h} c_\mathrm{h} - \mathsf{Q}_\mathrm{v}^\mathrm{T} \mathsf{H}_\mathrm{v} c_\mathrm{v} & \mathsf{N}_\mathrm{h} + \mathsf{N}_\mathrm{v} \\ e^\mathrm{T} \mathsf{G}_\mathrm{h} e & e^\mathrm{T} \mathsf{G}_\mathrm{v} e & e^\mathrm{T} \mathsf{H}_\mathrm{h} e + e^\mathrm{T} \mathsf{H}_\mathrm{v} e & w_\mathrm{h}^\mathrm{T} - w_\mathrm{v}^\mathrm{T} \\ 0 & 0 & e_1^\mathrm{T} \mathsf{S}_\mathrm{h}^\mathrm{T} e e^\mathrm{T} \mathsf{T}_\mathrm{h} e_1 & c_\mathrm{h}^\mathrm{T} \mathsf{T}_\mathrm{h} e_1 e_1^\mathrm{T} \mathsf{S}_\mathrm{h}^\mathrm{T} \mathsf{Q}_\mathrm{h} \\ 0 & 0 & e_1^\mathrm{T} \mathsf{S}_\mathrm{v}^\mathrm{T} e e^\mathrm{T} \mathsf{T}_\mathrm{v} e_1 & -c_\mathrm{v}^\mathrm{T} \mathsf{T}_\mathrm{v} e_1 e_1^\mathrm{T} \mathsf{S}_\mathrm{v}^\mathrm{T} \mathsf{Q}_\mathrm{v} \end{bmatrix} \tag{42}$$

and the right hand side and vector of unknowns are given as

$$g = \begin{bmatrix} \mathsf{Q}_\mathrm{h}^\mathrm{T} \hat{\mathsf{F}}_\mathrm{h} c_\mathrm{h} - \mathsf{Q}_\mathrm{v}^\mathrm{T} \hat{\mathsf{F}}_\mathrm{v} c_\mathrm{v} \\ e^\mathrm{T} \hat{\mathsf{F}}_\mathrm{h} e + e^\mathrm{T} \hat{\mathsf{F}}_\mathrm{v} e \\ e_1^\mathrm{T} \mathsf{F}_\mathrm{h} e_1 \\ e_1^\mathrm{T} \mathsf{F}_\mathrm{v} e_1 \end{bmatrix} \quad \text{and} \quad \psi = \begin{bmatrix} z_\mathrm{h} \\ z_\mathrm{v} \\ \zeta \\ \lambda \end{bmatrix} . \tag{43}$$

Finally, we solve these equations for the parameter vector, ψ, as,

$$\psi = -\mathsf{W}^{-1} g . \tag{44}$$

These parameter values, z_h, z_v, ζ, and λ, are then substituted into the expressions for the pressure matrices P_h and P_v in Equations (34) and (35) to complete the potential reconstruction.

FIELD PRESSURE VALIDATION

In this section, our goal is to demonstrate the robustness of the presented algorithm. To do so, we focus on the vertical results only and we begin by investigating the algorithm capacity to derive the true physical velocity field in the $x-y$ plane. Thus, Fig. 1 shows the comparison between from the original PIV dataset in the vertical PIV plane and the numerical derivation from the pressure potential field derivation. The structure of the fluctuations are quasi identical with the original dataset, suggesting a close fidelity to the flow separation dynamic.

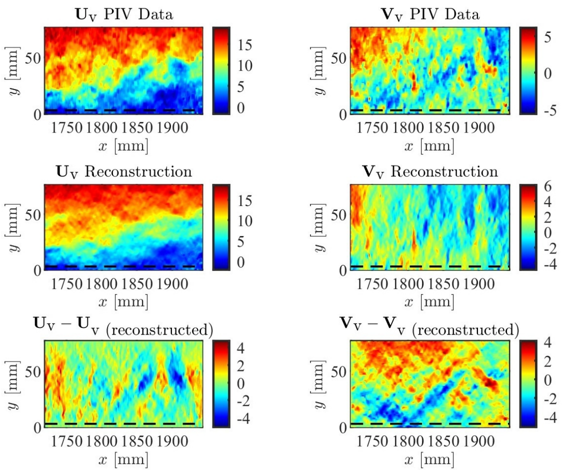

Figure 1. Main flow physics results from the vertical PIV dataset in both vertical (x-y) plane.

As an internal consistency check on the pressure reconstruction, we evaluate both sides of Eq. 8 in Van Oudheusden (2013) independently from the PIV data. The right-hand-side source term,

$$S_{2D}(x,y,t) = \left(\frac{\partial u}{\partial x}\right)^2 + 2\,\frac{\partial u}{\partial y}\,\frac{\partial v}{\partial x} + \left(\frac{\partial v}{\partial y}\right)^2, \tag{45}$$

is built solely from in-plane velocity gradients and is therefore unaffected by any integration or boundary-condition choice made in the pressure step. It thus offers a purely kinematic diagnostic of where the Poisson source is active. Because S_{2D} scales with the squared strain- and shear-rates, its temporal r.m.s. is expected to peak in regions of intense mean shear—most prominently along the separated shear layer. The r.m.s. field of S_{2D}, together with that of $|S_{2D}|$, exhibits exactly this signature, confirming that the velocity-derived source carries the correct spatial structure prior to any comparison with the reconstructed pressure.

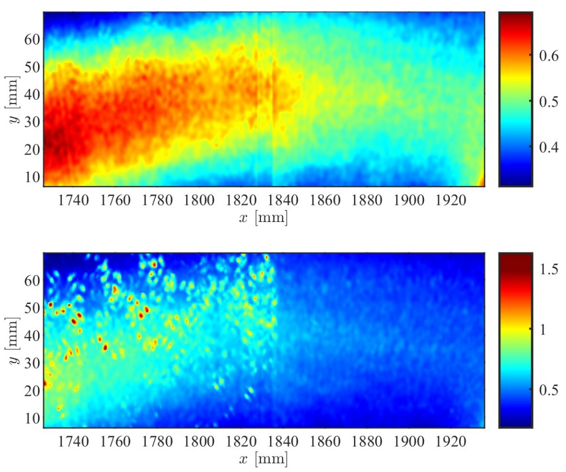

Figure 2. Poisson source terms computed from the pressure potential (top) and from the PIV data (bottom).

Figure 2 closes the loop by contrasting this raw velocity-based source with the Laplacian $\nabla^2\tilde{p}$ obtained from the reconstructed pressure potential. The two fields are computed from the same PIV snapshots through entirely independent operations: $\nabla^2\tilde{p}$ inherits the regularity of the least-squares pressure solver, whereas the right-hand side of Eq. 8 retains the full small-scale content of the velocity gradients. Despite this asymmetry, both fields collapse onto the same large-scale distribution and recover the shear-layer peak at the same streamwise location, with the residual differences confined to the high-wavenumber range where gradient amplification of PIV noise is expected to dominate. This agreement supports the interpretation that the 2D reconstructed pressure faithfully reproduces the kinematic forcing of the incompressible Poisson equation and is not biased by the boundary treatment of the solver, in spite of known limitations as discussed by Van Oudheusden (2013).

Fig. 3 shows the main flow physics with the mean streamwise and wall-normal velocity maps that hightlight the lift-up of the shearlayer. Of interest, the $rms(u)$ as well as the TKE computed using u^2+v^2 both allow to visibly identify the central region of that shear layer that produces the flow unsteady signatures.

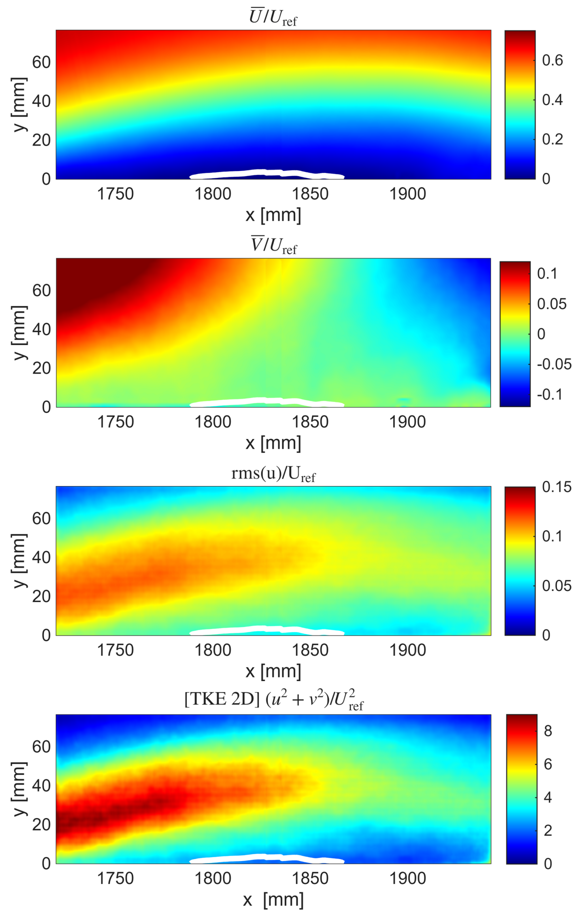

Figure 3. Main flow physics results from the vertical PIV dataset in both vertical (x-y) plane.

We directly compare these velocity topologies with the pressure field statistics shown in Fig. 4, where the top subplot first shows the mean pressure field map. These contours remarkably capture the same features as in Abe (2019) where the separation region shows a globally low pressure zone, with a moderate increase of field pressure inside the mean recirculation.

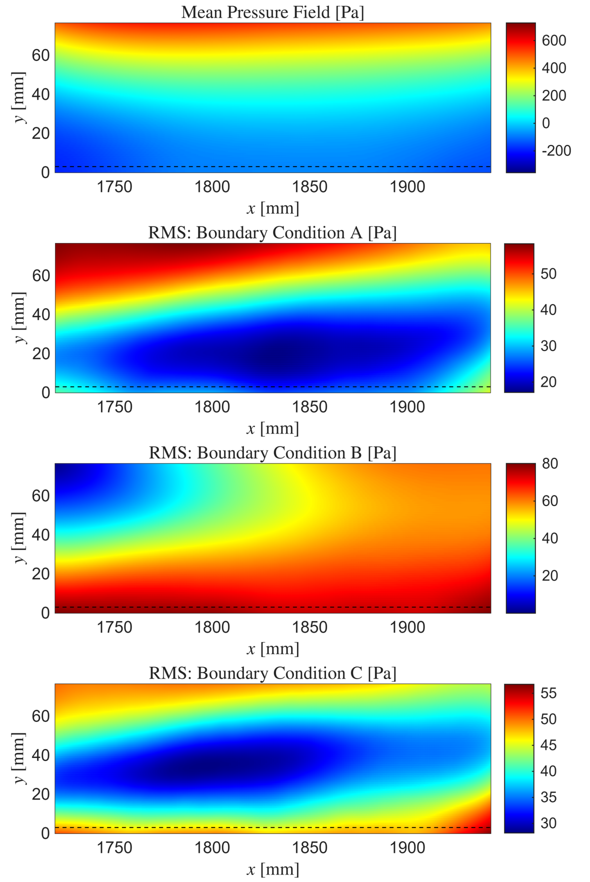

Figure 4. Main flow physics results from the vertical PIV dataset in both vertical (x-y) plane.

Three boundary-condition closures (A, B, C; Fig. 4, bottom) were compared. Case A enforces zero pressure averages along both horizontal and vertical edges of the FOV. Cases B and C instead anchor the reconstruction at the top-left corner, where the TKE is minimum (Fig. 3) and the flow approaches a potential-like state: case B subtracts the full corner pressure from the entire map, while case C removes only its low-frequency component, effectively acting as a high-pass filter on the field. The three closures yield mutually inconsistent r.m.s. topologies, with the peak fluctuation alternately localized near the potential-flow boundary (top of FOV) or near the wall (bottom of FOV). None reproduces the canonical APG signature reported by Abe (2019), in which the pressure fluctuation activity forms a coherent lobe above the TSB. This sensitivity reflects the under-determined nature of the boundary closure rather than a limitation of the integration scheme itself.

CONCLUSION

We have demonstrated a pressure-reconstruction algorithm whose accuracy on the Poisson problem is no longer the limiting factor: the residual uncertainty is concentrated in the boundary closure, which PIV-internal anchors alone cannot resolve. Lifting this ambiguity is the immediate next step. By incorporating synchronized wall-pressure measurements as an external Dirichlet constraint, we aim to recover a physically consistent field that reproduces the expected APG topology. The reconstructed pressure will then feed a modal (SPOD) decomposition targeting the low- and mid-frequency dynamics of the TSB—respectively associated with breathing and vortex shedding—thereby connecting the off-wall pressure organization to the measured wall-pressure signature.

REFERENCES

Abe, H. 2017 Reynolds-number dependence of wall-pressure fluctuations in a pressure-induced turbulent separation bubble. *Journal of Fluid Mechanics* **833**, 563–598.

Abe, H. 2019 Direct numerical simulation of a turbulent boundary layer with separation and reattachment over a range of reynolds numbers. *Fluid Dynamics Research* **51** (1), 011409.

Burden, R.L. & Faires, J.D. 2005 *Numerical Analysis*, eighth edn. Thomson Learning, Inc.

Chen, L. & Ye, Q. 2024 PIV-based fast pressure reconstruction and noise prediction of tandem cylinder configuration. *Experiments in Fluids* **65** (6), 98.

Harker, M. 2025 Least-squares reconstruction of a 3d potential from its measured spatial velocity field. In *Proceedings of the CSME-CFDSC-CSR 2025 International Congress*.

Harker, M. & O'Leary, P. 2015 Regularized reconstruction of a surface from its measured gradient field. *Journal of Mathematical Imaging and Vision* **51** (1), 46–70.

Le Floc'h, A. 2021 Experimental analysis in a family of turbulent separation bubbles. PhD thesis, École de technologie supérieure.

Le Floc'h, A., Mohammed-Taifour, A., Dufresne, L. & Weiss, J. 2018 Spanwise aspects of unsteadiness in a pressure-induced turbulent separation bubble. In *2018 Fluid Dynamics Conference*, p. 3538.

Le Floc'h, A., Suryadi, A., Hu, N., Herr, M., Wang, S., Ghaemi, S., Vétel, J., Di Labbio, G. & Dufresne, L. 2024 Wall pressure signature of separated flows: A comparison between flat plate and airfoil. In *Proceedings of the 13th International Symposium on Turbulence and Shear Flow Phenomena (TSFP13)*. Montreal, QC, CA.

Mohammed-Taifour, A. & Weiss, J. 2016 Unsteadiness in a large turbulent separation bubble. *Journal of Fluid Mechanics* **799**, 383–412.

Pröbsting, S., Tuinstra, M. & Scarano, F. 2015 Trailing edge noise estimation by tomographic particle image velocimetry. *Journal of Sound and Vibration* **346**, 117–138.

Schönemann, P.H. 1985 On the formal differentiation of traces and determinants. *Multivariate Behavioral Research* **20**, 113–139.

Van Oudheusden, BW 2013 Piv-based pressure measurement. *Measurement Science and Technology* **24** (3), 032001.

Wang, S., Gibeau, B. & Ghaemi, S. 2024 The interaction between turbulent separation bubble breathing and wall pressure on a 2d wing. *Experiments in Fluids* **65** (7), 99.